Journal of The
Electrochemical Society

Study of Solid-State Diffusion Impedance in Li-Ion Batteries Using Parallel-Diffusion Warburg Model

Journal of The Electrochemical Society, 2024 **171** 060539

Study of Solid-State Diffusion Impedance in Li-Ion Batteries Using Parallel-Diffusion Warburg Model

Xinhua Zhu,[1,z] Marta Cazorla Soult,[1,2] Benny Wouters,[1] and Mesfin Haile Mamme[1]

[1]*Department of Materials and Chemistry, Research Group Electrochemical and Surface Engineering, Vrije Universiteit Brussel, Brussels 1050, Belgium*
[2]*Imec, Kapeldreef 75, Leuven 3001, Belgium*

Anomalous diffusion impedance due to the solid-state Li^+ diffusion in Li-ion batteries is often troublesome for the analysis. In this work, we propose a novel analytical Parallel-diffusion Warburg (PDW) model and couple it with the conventional equivalent electrical circuit model (EECM) analysis to tackle this long-standing challenge. The analytical expression of the PDW is derived from the classical Fickian diffusion framework, introducing non-unified diffusion coefficients that originate from the diverse crystalline conditions of Li^+ diffusion paths, as theoretically demonstrated in the atomistic modeling results. The proposed approach (EECM + PDW) is successfully employed to study the diffusion impedance of thin-film $LiNi_{0.5}Mn_{1.5}O_4$ (LNMO) electrodes and porous $LiNi_{0.80}Co_{0.15}Al_{0.05}O_2$ (NCA) electrodes, demonstrating the applicability and robustness of this method.
 [DOI: 10.1149/1945-7111/ad5707]

Manuscript submitted March 16, 2024; revised manuscript received May 26, 2024. Published June 28, 2024.

Supplementary material for this article is available online

Electrochemical impedance spectroscopy (EIS) is a robust characterization tool for lithium-ion batteries (LIBs). It has been extensively used to investigate new battery materials,[1] and in recent years, it also has been proposed as an essential building block for next generation of battery management systems.[2–5] Thanks to modern EIS instrumentation, a single EIS measurement can sweep a broad frequency range, capturing the characteristic frequency responses associated with essential electrochemical processes within a battery system. However, analysis of EIS data often focuses on the high to intermediate frequency ranges, which are related to the dielectric properties of battery components and the charge-transfer process, respectively. On the other hand, impedance associated with mass transport phenomena in the low frequency range is often deprioritized or completely overlooked.[6–8] This trend can primarily be attributed to the presence of anomalous solid-state diffusion impedance in LIBs at low frequency ranges, which deviates from the standard finite-space Warburg (FSW) diffusion model based on Fickian diffusion.[9–11]

In literature, different approaches have been proposed to tackle the anomalous solid-state diffusion impedance in LIBs. Several works[12–14] have achieved good fitting results by introducing fractal finite-space Warburg (f-FSW) model (also known as generalized finite-space Warburg, GFW[15,16]) in the electrical equivalent circuit model (EECM). The fractal Warburg model is developed based on the mathematical description from Bisquert and Compte.[17] The underlying physical interpretation can be associated with non-Fickian diffusion with the presence of dissipative processes such as trapping and/or recombination in a disordered media.[18] Macdonald et al.[19,20] proposed a more robust theoretical framework of f-FSW based on Poisson Nernst Planck equations, but its application to battery systems has not yet been explored. In general, the f-FSW model can be nicely fitted to the anomalous diffusion impedance of LIBs; however, it has not been extensively adopted by researchers due to the dimensional issue of the obtained diffusion coefficient. Further investigation is needed, along with more accessible methods for determining or extracting the relevant physical parameters.

Another common approach is based on Fickian diffusion theory, where the anomalous diffusion behavior is originated from inhomogeneous diffusion paths.[21–24] Levi et al.[21] and Osaka et al.[22] have proposed to incorporate more than one Warburg element in EECM to tackle the anomalous diffusion impedance. This empirical adaptation is easy to implement and leads to good fitting results, but this comes at the cost of physical interpretability. Diard et al.[23] proposed using a log-normal distribution of diffusion lengths to describe the inhomogeneous diffusion behavior, and theoretical expressions of diffusion impedance were derived accordingly. Later, Song et al.[24] took both distribution of diffusion lengths and diffusion geometry into account for the Warburg diffusion model, which was validated on Si nanowire electrodes. In practice, the estimation of the distribution of diffusion lengths as well as the diffusion geometry from LIBs is extremely challenging. Lately, Min et al.[25] revealed that the characteristic diffusion length is independent from the secondary particle size for $Li(NiMnCo)O_2$ (NMC) cathode materials by conducting advanced single particle measurements. They attributed this unexpected observation to the cracks formation and electrolyte penetration on the secondary NMC particles as discussed in many previous studies.[26–28] This could result in shorter diffusion lengths, and irregular diffusion geometry.

Moreover, the porous electrode structure in practical LIBs further complicates the analysis of the diffusion impedance.[21,29–34] Sikha and White[29,30] derived an analytical impedance model taking into account the porous structure, the solution-phase diffusion and the solid-state diffusion. On the basis of the Sikha-White model, Woillez et al.[34] proposed a simplified framework to analyze the convoluted diffusion impedance of LIBs, which consists of solid-state diffusion and liquid-phase porous diffusion. Although the analytical model provides a robust way to analyze impedance data of LIBs, it requires specific input parameters of the studied system which are often not accessible in most application scenarios. Huang[35] extends the fractal diffusion theory to study space-domain fractal diffusion in porous electrodes. This work reveals the fractal dimensionalities of porous electrode in electrochemical devices.

In this work, we revisit the rudimentary approach of using a thin-film electrode system to study solid-state diffusion impedance of the state-of-the-art $LiNi_{0.5}Mn_{1.5}O_4$ (LNMO) electrode materials. Thanks to the well-defined diffusion length and geometry of the thin-film configuration coupled with the advancements of modern characterization techniques, the anomalous diffusion impedance is associated with inhomogeneous solid-state diffusion coefficients originating from different diffusion paths. Atomistic simulation results further suggest the presence of fast grain-boundaries diffusion and slow lattice diffusion within LNMO cathode materials. Moreover, a parallel-diffusion Warburg (PDW) model is proposed to quantify the different solid-state diffusion coefficients. The applicability the

[z]E-mail: Xinhua.Zhu@vub.be

PDW model is validated on both thin-film LNMO electrodes and thin-coated commercial $LiNi_{0.80}Co_{0.15}Al_{0.05}O_2$(NCA) electrodes.

Experimental

Electrode preparation.—Thin film LNMO electrodes were fabricated using an radio frequency sputtering technique (K. J. Lesker, Germany) under argon protected atmosphere. The process initiated with plasma ignition under an argon flow at 10 mTorr at a forward power of 40 W. The power was then gradually increased to 55 W at a rate of 0.033 W/s for the deposition of the LNMO layer, conducted at a reduced Ar pressure of 3 mTorr. Prior to deposition, a 10 minute pre-sputtering step was employed. After the deposition, the samples underwent an annealing process in air at 700 °C for one hour. The LNMO material was layered over a 70 nm thick Pt current collector. There is also a 20 nm TiO_2 interlayer between the Pt layer and the SiO_2/Si wafer substrate to ensure adhesion.

NCA electrodes were harvested from commercial pouch cells followed the established procedures.[8] Firstly, the commercial cell was fully discharged and transferred to an argon-filled glove box (Jacomex). Inside the glove box, the cell case was opened to extract the NCA electrode sheets. These sheets were then thoroughly washed in dimethyl carbonate (DMC). Following this, cotton swabs soaked in N-methyl-2-pyrrolidone were used to delicately remove the electrode coating from one side of a double-coated electrode sheet. After this process, several round NCA electrodes were cut to into disc with diameter of 18 mm and an area of 2.545 cm^2, from the treated electrode sheet. These electrodes were rinsed twice in DMC and subsequently left to dry under vacuum conditions for an entire night. The preparation of two identical NCA electrodes at different states of charge (SOC) was carried out in the following manner: Firstly, two harvested 18 mm NCA electrodes were each placed into separate three-electrode cells (EL-CELL, Germany), using lithium as both the counter electrode (CE) and reference electrode (RE). Secondly, these cells underwent 10 cycles of charging at a constant current (1C) at ambient temperature. Thirdly, during the final discharge cycle, the NCA electrodes were brought down to predetermined SOC levels ranging from 20% to 100%, as determined by the coulomb counting method. This was followed by a relaxation period of three hours. Finally, the identical NCA electrodes were carefully extracted from the three-electrode cells in a glove box. They were then promptly reassembled, along with new electrolyte and a separator, into a two-electrode symmetric cell. It was noted that the potential difference between the electrodes was less than 5 mV.

Experimental characterization.—The Scanning Electron Microscopy (SEM) image of the thin-film LNMO electrode was captured using a Nova 600 NanoLab. An in-house designed 3-electrode electrochemical-ellipsometry cell (Redox.me) was used for cyclic voltammetry (CV), galvanostatic cycling, and EIS characterizations. In this work, we exploited only the air-tight feature of the cell. For relevant ellipsometry studies, we direct readers to our previous works.[36,37] The electrochemical-ellipsometry cell was assembled inside an Ar-filled glove box (Jacomex) with thin-film LNMO as the working electrode (WE), Li metal as both CE and RE, and 1 M $LiPF_6$ in propylene carbonate (PC) as the electrolyte. The geometrical surface area of WE is 1.13 cm^2 (12 mm diameter). Potentiostatic EIS measurements were carried out using BioLogic SP-200 potentostat with a 7.07 mV root-mean-squre (RMS) amplitude and a frequency range of 10 mHz to 200 kHz. Due to the pronounced self-discharge rate of the thin-film LNMO electrode,[37] EIS was conducted at a quasi-steady state after holding at the designated potential levels for 30 minutes. After the EIS measurement, the electrode was (galvanostatically) charged to the next target potential level. All the potential values appeared in this work are versus Li/Li^+.

The SEM images of NCA electrodes were captured using a JEOL JSM-IT300. All NCA electrodes were tested in a commercial EL-CELL with two- or three-electrode configurations. Lithium metal served both as CE and RE. A 1.5 mm thickness glassy fiber (Whatman) separator was used. The cell was filled with 0.5 ml of LP30 (Ube Industries) electrolyte, which consists of 1M $LiPF_6$ in ethylene carbonate and DMC with 1:1 ratio by volume. Odd random phase EIS (ORP-EIS)[8,38,39] was conducted on the NCA symmetrical cells using an in-house built setup consisting of a Wenking Potentiostat POS 2 (Bank Elektronik) and a PCI-4461 DAQ-card (National Instruments). A frequency range of 3 mHz to 5 kHz and an RMS amplitude of 5 mV were chosen for the experiments.

EIS data analysis.—EIS data of thin-film LNMO were validated using linear Kramers-Kronig (lin-KK) test[40] through the open-source Python package impedance.py.[41] EIS data of NCA were validated using the default error analysis of the ORP-EIS technique.[8] EIS data of thin-film LNMO at frequencies higher than 2 kHz, and EIS data of NCA at frequencies higher than 1 kHz were omitted for EECM modeling due to the potential instrumentation artifacts in the high-frequency impedance response.[5] The EECM analysis was performed using the in-house developed Python code, based on an open-source Python package **lmfit**.[42] This code employs non-linear least-squares regression of the circuit model to the impedance data, following the Levenberg-Marquardt optimization algorithm. The uncertainties of the best-fit parameters are estimated by inverting the Hessian matrix.

Computational methodology.—Lithium-ion diffusion can be accurately predicted through first-principal ab initio calculations. However, the computationally expense associated with these calculations, particularly when dealing with systems containing a large number of atoms, such as ours, can be prohibitive. Therefore, there is a compelling need for alternative approaches that can achieve comparable accuracy in significantly less time. To address this challenge, we utilized molecular dynamics simulations (MD) employing the dispersion-corrected M3GNet neural network potential,[43] using AMS software package.[44] This neural network potential has demonstrated excellent in describing various battery materials and was trained using first-principle ab initio calculations from the Materials project.[43,45] The validity of M3GNet neural network potential for LMNO simulation was confirmed as shown in Supplementary Materials (Fig. S1) by comparing with the corresponding first principle calculation using BAND planewave DFT code available in AMS software package.[44]

Building upon the prior report regarding grain boundaries simulation in lithium-ion battery cathodes,[46] we constructed a supercell featuring a tilt grain boundary (GB), specifically with low-index plane (Σ3 (011)[1-11]) contains 336 atoms, in accordance with the principle of coincidence site lattice (CSL) theory using QunatimATK software package,[47] and we have incorporated an optimized structural refinement process that encompasses multi-step. Initially, we employ MD techniques for annealing, cooling, and energy relaxation. Within these MD simulations, we implemented the canonical ensemble (NVT) coupled with a Nose-Hoover (NHC) thermostat and Martyna-Tobis-Klein (MTK) barostat to ensure stable temperature and pressure throughout.[48] The simulations are carried out using a time-step (Δt) of 1 fs. In this context, the MD simulations consist of three primary phases for the GB simulations: an annealing stage set at $T = 800$ K for 10 ps, succeeded by a constant temperature of 800 K for 10 ps and followed by stepwise quenching from 800 K to 0 K at a rate of 8×10^{14} Ks^{-1}. Subsequently, a 1 ps NVT simulation at $T = 0$ K is conducted to stabilize the system.

To determine the energy barrier for Li-ion migration, the climbing image nudged elastic band (CI-NEB) method as implemented in the transition state tools (VTST) for AMS software package is employed.[49] This method requires the initial and final diffusion states as input and generates intermediate states via linear interpolation of atomic coordinates. For the calculation, we used a spring constant of 1 Hartree/$Bohr^2$.

Results and Discussion

EIS characterization of the thin-film LNMO electrode.—Thin-film intercalating electrodes provide the simplest configuration and a robust approach to study the solid-state diffusion phenomena.[9,50] In this work, we have combined the thin-film configuration with the next-generation cobalt-free LNMO cathode material to revisit solid-state diffusion impedance, a long-lasting puzzle of LIBs. Thin-film LNMO electrodes were prepared and comprehensively characterized by various surface and electrochemical techniques. The basic electrochemical characteristics of the electrode are presented in the CV and the galvanostatic cycling results shown in Supplementary Materials (Fig. S2). More comprehensive discussion of these results have been reported in our previous work.[36,37] In this work, we focus mainly on its EIS data, particularly on the diffusion impedance at the low frequency range. Figure 1a shows the SEM image of the thin-film LNMO electrode, where a dense polycrystalline LNMO layer, approximately 80 nm thick, is coated on the Pt current collector. EIS is obtained at different electrode potential, i.e. SOC, shown in Figs. 1b and 1c. Due to the possible measurement artifacts in the high frequency range, the EIS analysis focus on the frequency range of 10 mHz to 2 kHz. The EIS spectra are fairly simple, consisting of one major time constant associated with kinetics at the high frequency region and a predominant diffusion impedance at the low frequency region. The outlier at 3.8 V, which equates to 0% SOC, exhibits significantly higher impedance with one convoluted time constant. Such EIS behavior is expected due to the sluggish kinetics at low SOC.[8] Starting from 4.2 V onward, the kinetics-related impedance in the high frequency region decreases with elevated electrode potential (i.e. SOC). This can be associated with the intrinsic kinetic changes of the electrode materials. This is also the case for the state-of-the-art Ni-rich cathode materials.[5,8] The variation of the diffusion impedance at different SOCs is more complicated. Nevertheless, the anomalous diffusion impedance is present for all the potentials beyond 3.8 V as indicated in the Nyquist plot (b), where the Warburg tail deviates from a vertical line, or in the Bode-phase plot (c), the phase angle at the low frequency is plateaued deviates from $-90°$.

In this work, we address the diffusion impedance on the basis of Fickian diffusion framework, in which the origin the anomalous diffusion behavior is associated with inhomogeneous diffusion paths. In literature,[23,24] a log-normal distribution of the diffusion lengths is

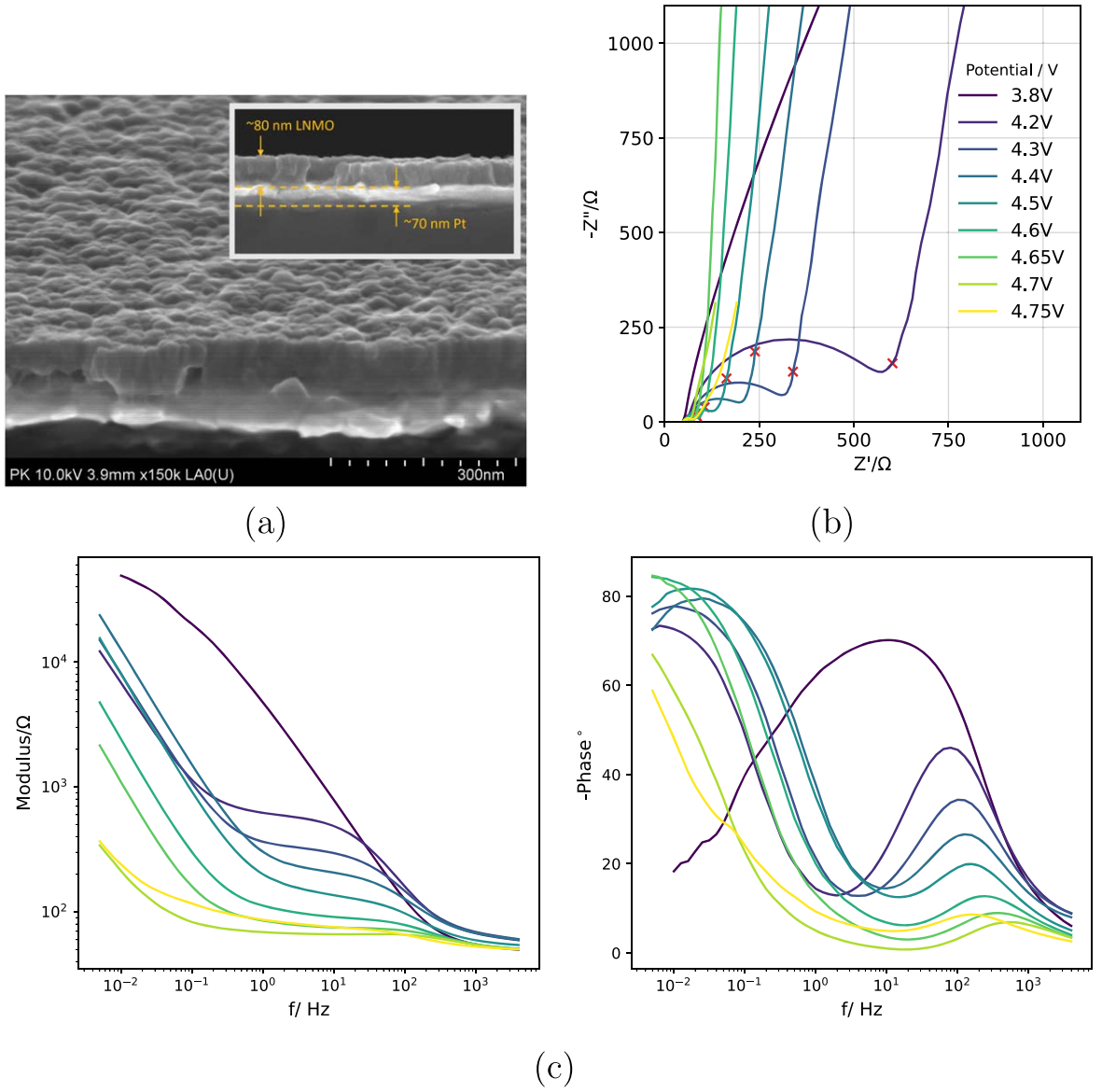

Figure 1. (a) SEM image of thin-film LNMO electrode; (b) Nyquist plot of EIS data at different potential; The red cross indicates the data at 1 Hz; (c) Bode plot of EIS data at different potential. Experimental conditions: RMS amplitude of EIS signal is 7.07 mV; frequency range is 0.01 Hz–2 kHz; temperature 22 ° C; the potential values are versus Li/Li^+.

incorporated into the diffusion model to model the inhomogeneous diffusion paths and the anomalous diffusion impedance. However, as shown in Fig. 1a, the LNMO electrode, as thin as 80 nm, unlikely exhibits a log-normal distribution of the diffusion lengths, we hence propose a different perspective by incorporating different solid-state diffusion coefficients as main cause of the anomalous diffusion impedance instead of different diffusion lengths.

It has been reported that the solid-state diffusivity can vary by several orders of magnitude between grain boundary (GB) diffusion and lattice diffusion in various solid-state systems.[51–53] Recently, He et al.[46] applied a first-principles theoretical approach to systematically study the Li diffusivity under different GB conditions in NMC cathode materials. In this work, we have adopted a similar atomistic approach to investigate Li diffusivity in LNMO cathode materials. The results are shown in Fig. 2, in which Li-ion migration pathway across Σ3 (011)[1-11] from site **A** to **F** is illustrated in (a), and the corresponding energy profiles for each step are plotted in (b). It is evident that Li ions need significantly less energy to migrate within GB (**C** to **D**) than within the bulk matrix (**A** to **B**, or **E** to **F**). Additionally, the two bulk-to-GB energy profiles (**B** to **C** and **D** to **E**) behave differently. The path of **D** to **F**, crossing Mn, presents a lower energy barrier than the path of **B** to **C**, which crosses Ni. Further investigations will be carried out to understand this interesting observation. In general, the computation results for LNMO are in line with other studies showing that GBs promote Li diffusivity. More GB conditions for LNMO are under investigation, and the comprehensive analysis will be reported elsewhere as an independent work.

Parallel-diffusion warburg model.—Informed by the insights gained from atomistic simulations, we proposed a novel Parallel-diffusion Warburg (PDW) model to address the anomalous diffusion impedance arising from the presence of different diffusion coefficients, which differ by orders of magnitude. We start from taking two discrete diffusion coefficients and a weighting factor into account in the PDW model for the simplest scenario. The mathematical expression of the PDW model is defined as follows:

$$Z_{pdw}(\omega) = \frac{RT}{z^2F^2\Lambda} \cdot \frac{1}{\theta\sqrt{j\omega\tilde{D}_1}\tanh\left(L\sqrt{\frac{j\omega}{\tilde{D}_1}}\right) + (1-\theta)\sqrt{j\omega\tilde{D}_2}\tanh\left(L\sqrt{\frac{j\omega}{\tilde{D}_2}}\right)} \quad [1]$$

and the lumped parameter

$$\Lambda = \frac{C_{eq}A}{\Gamma} \quad [2]$$

where z is the charge of the mobile ion; F, R, and T retain their usual meanings; j is the imaginary unit; ω is the angular frequency; L is the diffusion length; $\tilde{D}_1$ and $\tilde{D}_2$ are two solid-state diffusion coefficients; θ and $1-\theta$ are the surface coverage of $\tilde{D}_1$ and $\tilde{D}_2$, respectively; Γ is the Thermodynamic Factor, C_{eq} is the equilibrium Li^+ concentration, and A is the active surface area. In the context of solid-state diffusion, the diffusion coefficient often varies with concentration, and this relation can be accounted for by the Thermodynamic Factor.[50,54] Details of the derivation of Eq. 1 can be found in appendix. The exact physical definitions of the different diffusion coefficients are ambiguous. Based on the atomistic simulation results, we postulate that the higher diffusion coefficient is associated with grain-boundary diffusion, and the lower diffusion coefficient is associated with bulk diffusion. The surface coverage θ and $1-\theta$ work as weighting factors for the two diffusion processes with respect to the total diffusion impedance. It is important to note that the PDW is derived based on the framework of solid-state Fickian diffusion and finite-length Warburg.[9,50] Therefore, the application of the PDW is predicated on the following assumptions: (i) the electrode is a mixed ionic and electronic conductor, and the electronic conductivity is sufficiently large; (ii) the electrode potential is a measure of the lithium activity at the electrode/electrolyte interface; (iii) the mass transport is governed only by one-dimensional Fickian diffusion; (iv) the kinetic effects and mass transport effects are well-separated by frequencies; (v) liquid phase diffusion is neglected due to being faster by several orders of magnitude (Supplementary Materials Fig. S3); (vi) only planar diffusion geometry is considered

The essence of the PDW model is to average out the two independent diffusion coefficients $\tilde{D}_1$ and $\tilde{D}_2$, and the coverage θ serves as weighing factor for the two diffusion processes. When $\theta = 1$, Eq. 1 becomes

$$Z_{pdw}(\omega) = \frac{RT}{z^2F^2\Lambda} \cdot \frac{1}{\sqrt{j\omega\tilde{D}_1}\tanh\left(L\sqrt{\frac{j\omega}{\tilde{D}_1}}\right)} \quad [3]$$

which is identical to the FSW model.[9–11] Similarly when $\theta = 0$, same expression as Eq. 3 can be derived with the sole presence of $\tilde{D}_2$. Figure 3a provides an overview of impedance response of PDW and FSW. The simulation results are based on the Randles equivalent circuit[55] as shown in Fig. 3b. The blue solid line and the orange dotted line are simulated using Eq. 3 with $\tilde{D}_1$ and $\tilde{D}_2$, respectively. Here we assume $\tilde{D}_1 = 10^{-10}$ cm^2/s and $\tilde{D}_2 = 10^{-11}$ cm^2/s. The green dash line, exhibiting anomalous diffusion, is modeled using PDW (Eq. 1) with both $\tilde{D}_1$, $\tilde{D}_2$, and $\theta = 0.5$. By adjusting these three parameters, various anomalous diffusion impedance response can be simulated.

Application of the PDW Model to Thin-film LNMO Electrodes.—Complex nonlinear least square (CNLS) fitting can be applied on the EIS data of thin-film LNMO using the Radles equivalent circuit model with PDW as the diffusion model shown in Fig. 3b. It is important to mention that all EIS data was validated with the lin-KK test.[40,41] The EIS data at 3.80 V, 4.70 V and 4.75 V failed the lin-KK test (as shown in Supplementary Materials, Fig. S4). It is due to the highly non-linear behavior of the electrode when at 3.80 V, which correspond to about 0% SOC. The invalidity at 4.70 V and 4.75 V is attributed to the non-linearity and non-stationarity caused by side reactions, which has been systematically discussed in the previous work.[37] Therefore, the in-depth analysis was conducted on the remaining EIS data that passed the lin-KK test. Figure 4 shows the EIS data, fitting data, and fitting residual of the electrode charged to 4.65 V, which approximates to 20% to 30% SOC. In general, we achieved good overall fitting: the fitted parameter values and uncertainties are shown in Table I, and the goodness-of-the-fit can be assessed by the residual curve presented in the Bode modulus plot, which is approximately two orders of magnitude lower than the measured modulus. A higher discrepancy between the data and the fitting can be observed at the last few points in the low-frequency range, where the fitting data becomes a vertical line, but the experimental data still deviate from it. This could be an indication of a even slower diffusion phenomena that is neglected in the PDW model (Eq. 1). Consequently, we derived a new PDM-3D model (Eq. 4) with three diffusion coefficients and applied it to the same EIS data at 4.65 V, shown in Fig. 5.

$$Z_{pdw}(\omega) = \frac{RT}{z^2F^2\Lambda} \cdot \frac{1}{\theta_1\sqrt{j\omega\tilde{D}_1}\tanh\left(L\sqrt{\frac{j\omega}{\tilde{D}_1}}\right) + \theta_2\sqrt{j\omega\tilde{D}_2}\tanh\left(L\sqrt{\frac{j\omega}{\tilde{D}_2}}\right) + (1-\theta_1-\theta_2)\sqrt{j\omega\tilde{D}_3}\tanh\left(L\sqrt{\frac{j\omega}{\tilde{D}_3}}\right)} \quad [4]$$

The overall fitting residue is lower for PDM-3D model, particularly at the lower frequencies. Current fitting tool provides information of Akaike information criterion (AIC),[56] which suggests that PDM-3D, with a lower AIC values, perform slightly better than PDM model (AIC=-1021 for PDM-3D and AIC=-900 for PDM). However, the

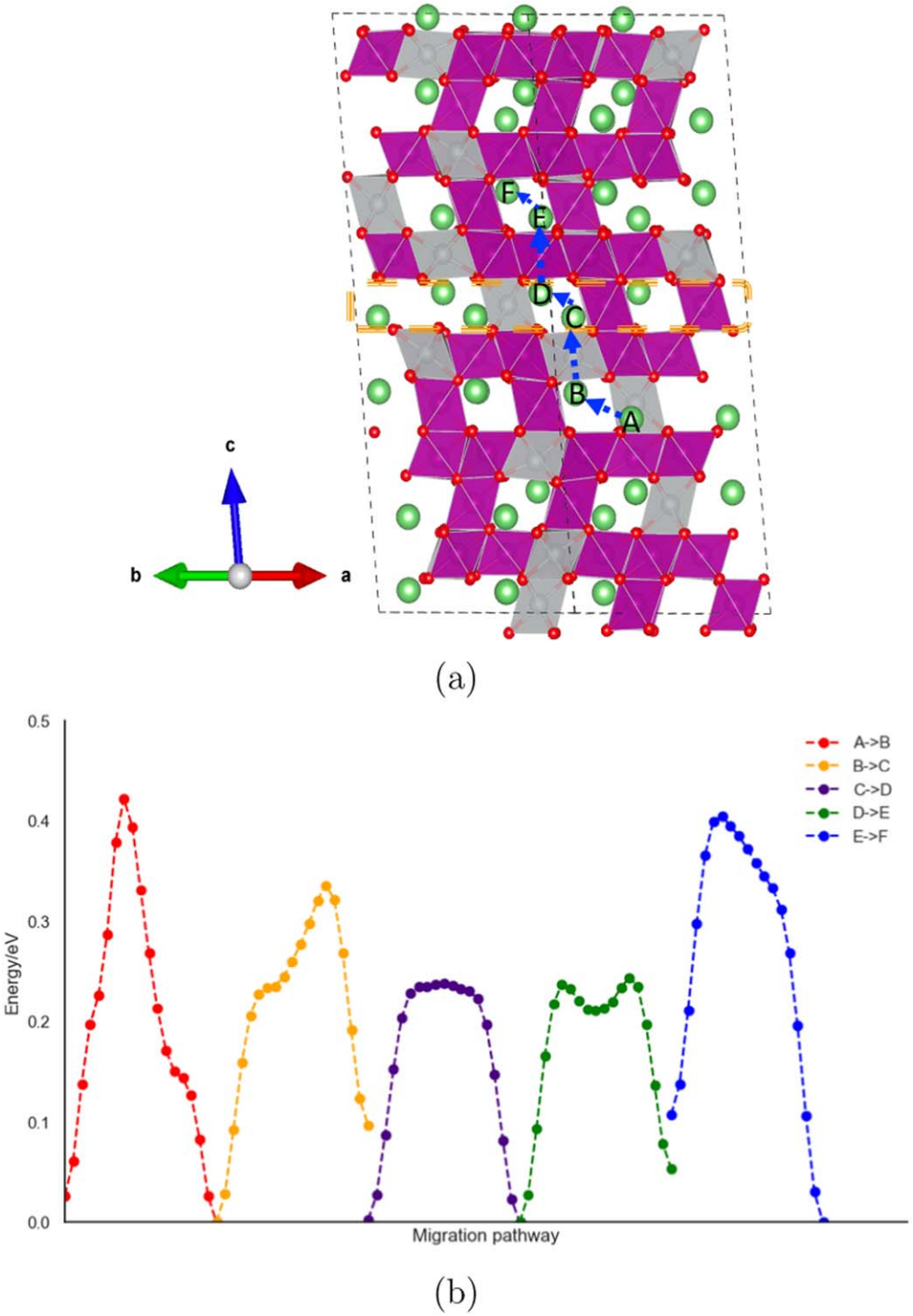

Figure 2. Li-ion migration pathway across Σ3 (011)[1-11] from the site **A** to **F** is illustrated in (a) and the corresponding energy profile within bulk (red and blue curve), bulk to grain boundary (orange and green) and grain boundary to grain boundary (purple) (b). The red, gray, purple, and green spheres represent the oxygen, nickel, manganese and lithium atoms, respectively.

uncertainties of the diffusion-related parameters (Table II) has increased likely due to the extra fitting parameter, $\tilde{D}_3$ and θ_2, are introduced.

Additionally, we carried out another fitting on the same impedance data with GFW model. The fitting results are shown in Supplementary Materials (Fig. S5) and compared with the results obtained from the PDW models (2D and 3D). GFW model achieves good approximations, but its fitting residual are higher than the those of the PDW models. Since the PDW models are more complex (with more fitting parameters) than the GFW model, an F-test[57] was performed between the PDW models and the GFW model, as shown in Supplementary Materials (Table S1). Both PDW models passed the F-test, so the extra parameters included in the PDW models compared to the GFW model are statistically justified. We also performed an F-test between PDW (2D) and PDW-3D, and PDW-3D also passed the test. However, due to the same arguments provided earlier, we still encourage the use of PDW (2D) at this stage.

We believe that the GFW (or fractional diffusion) model and the PDW model share the same fundamental basis, i.e. the diffusion process is non-unified and distributed: the fractionality of the GFW

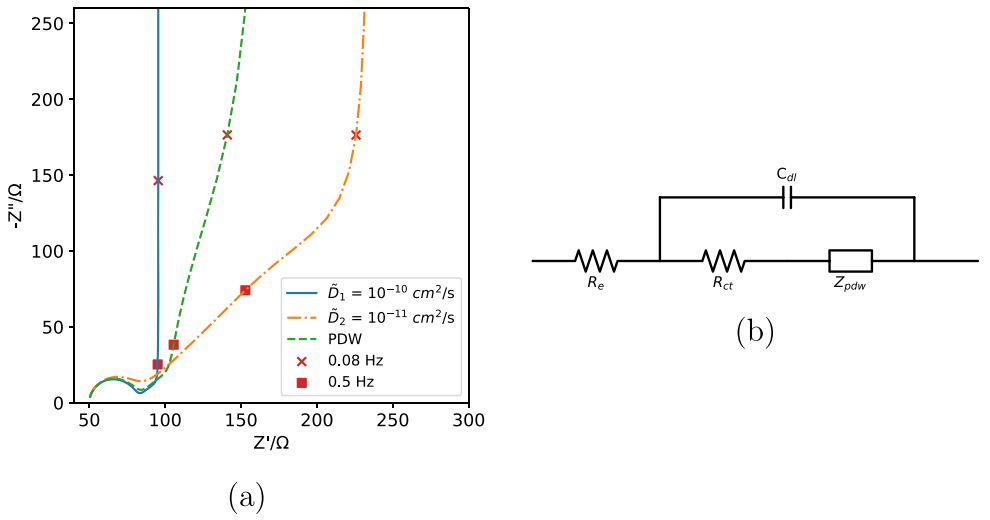

Figure 3. (a) simulation results with either single diffusion coefficient (Eq. 3) or two diffusion coefficients (Eq. 1); (b) the Randles equivalent circuit with PDW model integrated. Simulation parameters: $\tilde{D}_1 = 10^{-10}$ cm^2/s; $\tilde{D}_2 = 10^{-11}$ cm^2/s; $\theta = 0.5$; $L = 80$ nm; $T = 295.15$ K; $\Lambda = 4 \times 10^{-4}$ mol/cm; $Re = 50\ \Omega$; $R_{ct} = 30\ \Omega$; $C_{dl} = 20\ \mu F$; frequency 2 kHz–10 mHz.

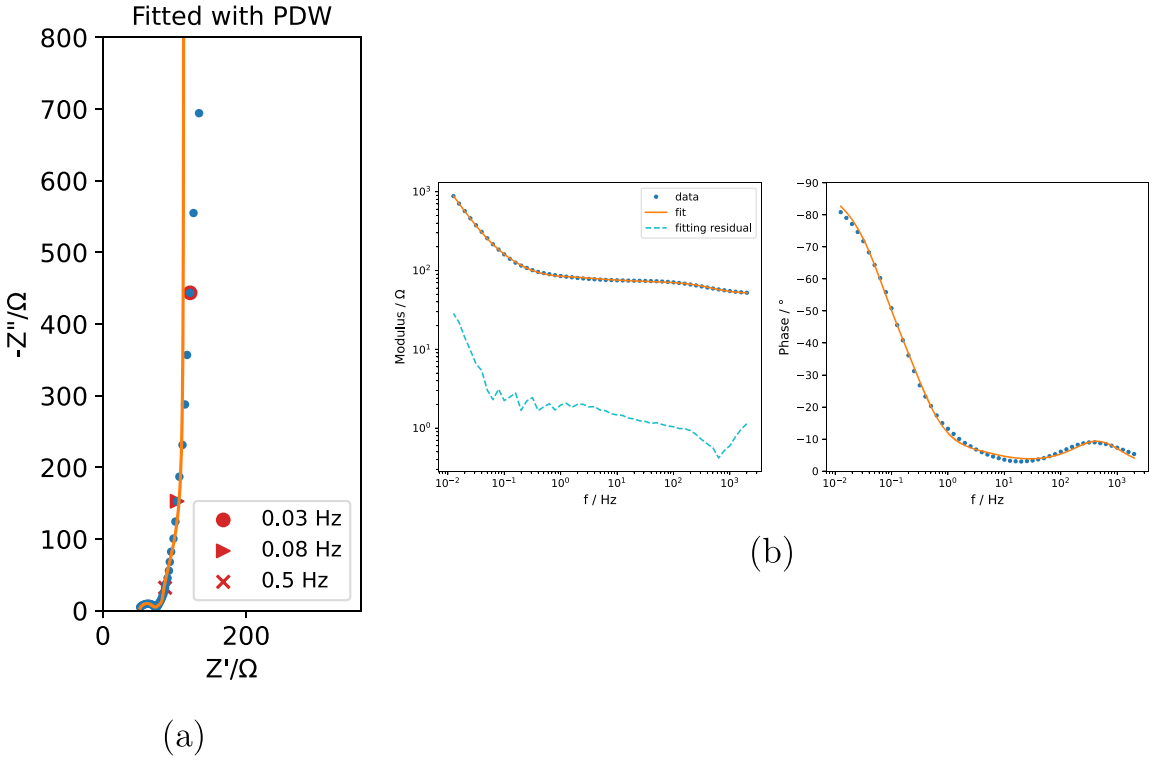

Figure 4. (a) Nyquist plot of EIS data at 4.65 V vs Li/Li^+, and its fitted data; (b) Bode plot of the EIS data, the fitted data and the fitting residual. The EIS data is fitted with the Randles circuit with PDW as the diffusion model; input parameters: $L = 80$ nm; $T = 295.15$ K. Experimental conditions: RMS amplitude of EIS signal is 7.07 mV; frequency range is 0.01 Hz–2 kHz.

model is often associated with the distributed diffusion length (L);[16,35] the PDW model is based on non-unified diffusion coefficients (D). For a thin-film system, the distributed D seems play a major role compare to L. On the other hand, with increasing the geometrical complexity, the L might eventually play the major role.

In conclusion, for thin-film electrodes the original PDW model with two diffusion coefficients is the most practical option. The application of PDM-3D could lead to improved fitting results but with an increasing risk of overfitting and the cost of interpretability. Alternatively, it will be interesting to introduce a probability density function (PDF) of the diffusion coefficient in the PDW to have a better description of the parallel diffusion impedance. This is the same approach as used in the previous work,[23,24] where a log-normal distribution of the diffusion lengths was introduced in the diffusion model. However, this brings a significant challenge being the determination of the PDF of the diffusion coefficient, which might be achieved through more extensive atomistic simulations. We will explore this topic in our future work.

In addition to the EIS data at 4.65 V, all other EIS data were fitted with the PDW model, and their fitting results are summarized in Table I. Although they generally show acceptable fitting qualities, the relative error (in brackets) increases with decreasing electrode

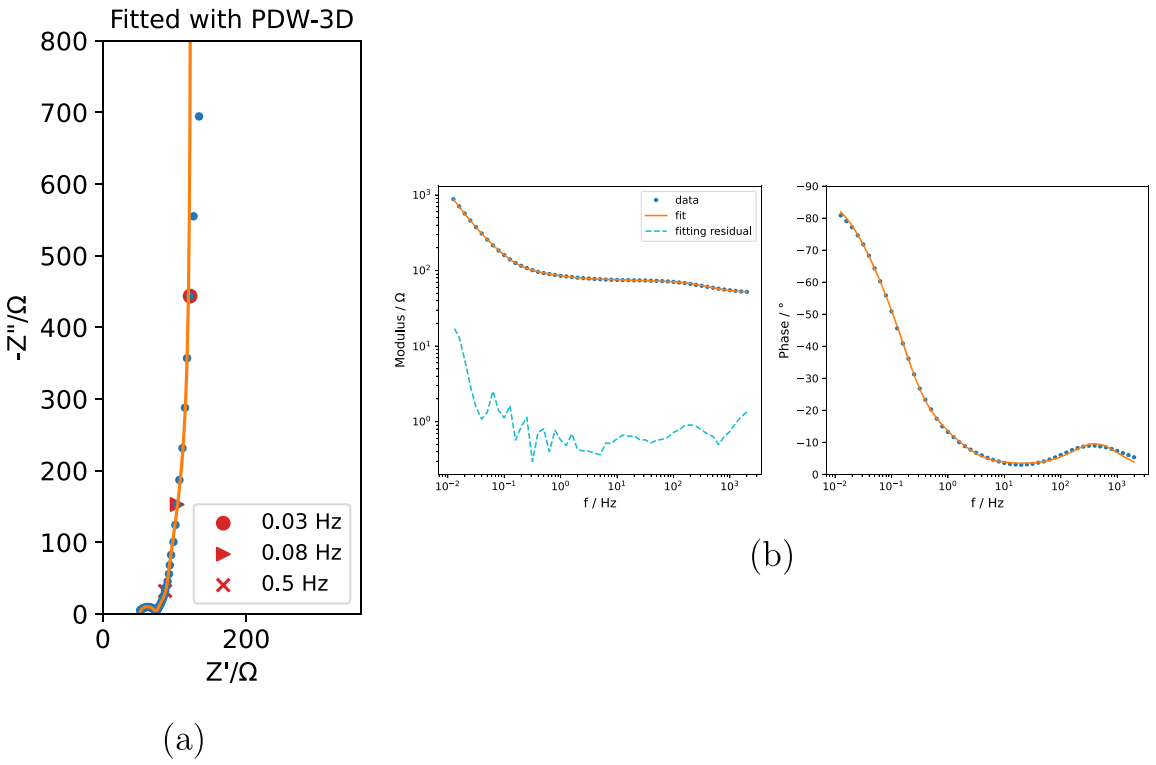

Figure 5. (a) Nyquist plot of EIS data at 4.65 V vs Li/Li$^+$, and its fitted data; (b) Bode plot of the EIS data, the fitted data and the fitting residual. The EIS data is fitted with the Randles circuit with PDW-3D as the diffusion model; input parameters: $L = 80$ nm; T=295.15 K. Experimental conditions: RMS amplitude of EIS signal is 7.07 mV; frequency range is 0.01 Hz–2 kHz.

Table I. Fitted parameter values and the relative errors (in brackets) at different electrode potential.

Parameter	4.2V	4.3V	4.4V
R_e (Ω)	65.97 (1.3%)	66.62 (1.1%)	64.22 (1.2%)
C_{dl} (F)	1.18×10^{-5} (1.6%)	1.23×10^{-5} (2.0%)	1.30×10^{-5}(2.8%)
R_{ct} (Ω)	400.49 (1.6%)	188.41 (1.7%)	99.44 (2.2%)
D_1 (cm^2/s)	6.14×10^{-11} (8.2%)	1.41×10^{-10}(6.8%)	2.92×10^{-10} (5.8%)
D_2 (cm^2/s)	2.59×10^{-12} (20.6%)	4.24×10^{-12} (15.0%)	5.47×10^{-12} (13.0%)
θ (-)	0.58 (4.7%)	0.65 (2.9%)	0.67 (2.3%)
Λ (mol/cm)	7.81×10^{-5} (4.4%)	6.16×10^{-5} (2.4%)	3.90×10^{-5} (1.9%)
Parameter	4.5V	4.6V	4.65V
R_e (Ω)	56.47 (0.9%)	52.07 (0.6%)	51.34 (0.7%)
C_{dl} (F)	1.73×10^{-5} (3.2%)	2.04×10^{-5} (3.3%)	2.06×10^{-5} (4.6%)
R_{ct} (Ω)	52.77 (2.1%)	28.88 (1.6%)	19.04 (1.9%)
D_1 (cm^2/s)	2.89×10^{-10} (5.3%)	1.87×10^{-10} (4.9%)	1.67×10^{-10} (6.3%)
D_2 (cm^2/s)	1.80×10^{-11} (9.6%)	1.83×10^{-11} (6.7%)	1.65×10^{-11} (6.1%)
θ (-)	0.67 (2.2%)	0.62 (2.5%)	0.58 (2.9%)
Λ (mol/cm)	5.75×10^{-5}(0.9%)	1.91×10^{-4} (0.6%)	4.22×10^{-4} (0.6%)

potentials. This can be attributed to the sluggish kinetics at lower electrode potentials, which deviate from the basic assumptions of PDW. In Fig. 6a, the charge transfer resistance R_{ct} significantly increases with lower electrode potentials. The application of PDW should avoid SOC regions with sluggish kinetics, occurring often in low SOC or very high SOC regions.[8] In these regions, the assumption related to the solely diffusion-controlled process might be violated. The double layer capacitance C_{dl} shows reasonable values that are in line with the theoretical expectations (10 to 40 $\mu F/cm^2$[58]). C_{dl} exhibits a steep increase from 4.4 V to 4.6 V, indicating drastic changes in surface conditions of LNMO. It could be related to the major phase transition of LNMO electrodes starting at the same potential window, as shown in the CV, Supplementary Materials (Fig. S2). Figure 6b presents the plot of the fitted PDW parameters as a function of electrode potentials. Although D_1 is generally one order of magnitude higher than D_2, D_1 and D_2 vary similarly across different electrode potentials. The faster diffusion coefficient, D_1, is attributed to grain boundary diffusion, while D_2 is attributed to lattice diffusion. The coverage θ and $1-\theta$ are associated with D_1 and D_2, respectively, showing that the grain boundary diffusion plays a major role at every potential. Similarly to the diffusion coefficients, the coverage values also vary with

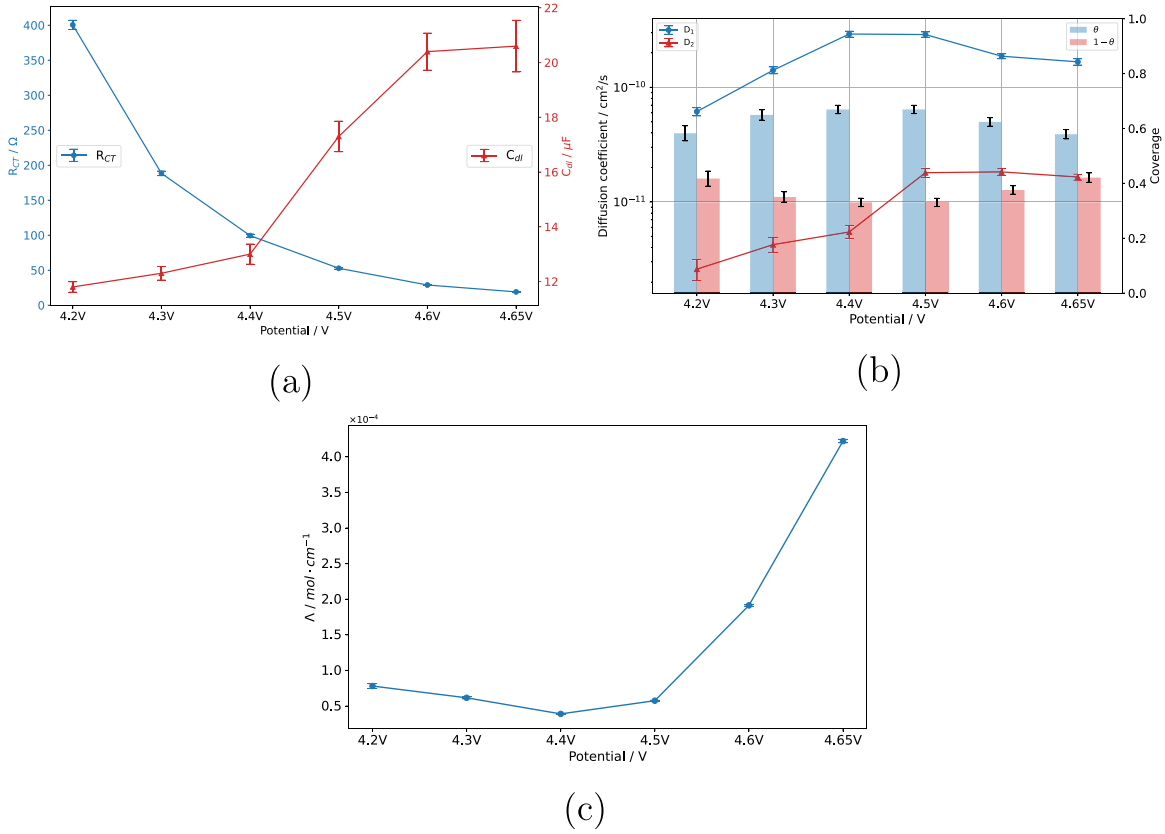

Figure 6. Plot of the fitted parameters and their standard deviation as function of electrode potentials. (a) R_{ct} and C_{dl}; (b) D_1, D_2 and θ; (c) the lumped parameter Λ.

Table II. Fitted parameter values and the relative errors (in brackets) with different PDW model for the thin-film LNMO electrode at 4.65 V vs Li/Li$^+$.

Parameter	PDW	PDW-3D
R_e (Ω)	51.34 (0.7%)	51.64 (0.4%)
C_{dl} (F)	2.06×10^{-5} (4.6%)	2.18×10^{-05} (2.5%)
R_{ct} (Ω)	19.04 (1.9%)	19.76 (1.1%)
D_1 (cm^2/s)	1.67×10^{-10} (6.3%)	6.64×10^{-10} (12.8%)
D_2 (cm^2/s)	1.65×10^{-11} (6.1%)	7.20×10^{-11} (5.6%)
D_3 (cm^2/s)	–	9.25×10^{-12} (6.5%)
θ_1 (-)	0.58 (2.9%)	0.22 (7.0%)
θ_2 (-)	–	0.51(2.9%)
Λ (mol/cm)	4.22×10^{-4} (0.6%)	4.29×10^{-4} (0.4%)

electrode potentials. Further dedicated investigations, coupled with other characterization techniques, are needed to fully understand the changes in D_1, D_2, and θ as a function of electrode potentials. Figure 6c shows the plot of the lumped parameter Λ, which also varies with different electrode potentials. According to Eq. 2, Λ is a function of equilibrium Li^+ concentration (C_{eq}), active surface area (A) and Thermodynamic Factor (Γ). When increasing the electrode potential (i.e.bringing LNMO electrode to a higher SOC), C_{eq} decreases, leading to a drop in Λ. However, as shown in Fig.6c, Λ first decreases, then an increase occurs at potentials above 4.5 V, which corresponds to the electrochemical active region of the LNMO electrode as shown in Supplementary Materials (Fig. S2). This could be related to the Thermodynamic Factor Γ due to phase changes in the LNMO electrode. Additionally, the increase in the Λ could also be associated with change in the active surface area A due to cracks formation during the initial delithiation process.[36,37]

In summary, we have demonstrated that PDW can be easily implemented in classical EECM analysis. The fitted parameters of PDW derived from the thin-film LNMO electrode are consistent and physically relevant. A systematic study of these parameters, along with the cycling aging of cathode materials, could be very interesting and is planned for future research. Additionally, we discussed how PDW can be converted into PDW-3D for a more accurate fitting of diffusion impedance, however, in practice, this approach is discouraged due to the limited number of data points accessible in the low-frequency range. Nevertheless, the discussion highlights that the essence of PDW is to account for different diffusion coefficients. The number of diffusion coefficients could be two, three, or even a PDF if determinable in future studies.

Application of PDW model to commercial NCA electrodes.—The application of PDW has been demonstrated on the study of thin-film

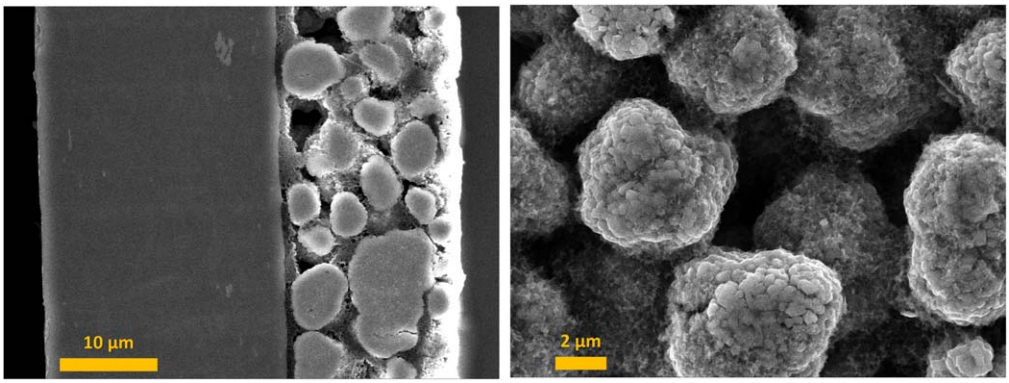

Figure 7. SEM images of the porous NCA electrode: (a) cross-section area; (b) top-view morphology.

LNMO electrode with well-defined diffusion geometry and thickness. However, the preparation of thin-film electrodes requires sophisticated processes and tools, which are not accessible to most researchers. Therefore, we further demonstrate the use of the PDW model to study commonly used porous electrodes. The porous NCA electrodes were harvested from power-optimized commercial batteries. As shown in Fig. 7a, approximately 10 to 15 μm of active porous layer was coated on the Al current collector due to the high-power design. Previous studies[34,59] reveal that the porous structure significantly complicates impedance response, particularly the low-frequency regions. The thin porous electrode design can minimize the porous diffusion and approximate the boundary conditions predicted by the PDW model. Nevertheless, the use of PDW model can significantly simplify the diffusion geometry, which should be applied very cautiously when used for porous electrodes. Figure 7b shows the morphology of the NCA electrode consisted of sphere-like secondary particles with radius around 2 to 5 μm. The secondary particles are agglomeration of much smaller primary particles, which is about 100 to 300 nm length. Estimating the diffusion length is more troublesome compared to thin-film electrodes. The radius of secondary particles is often used as the diffusion length to quantify diffusion coefficients in literature. However, a recent study[25] shows that the diffusion length is independent of the secondary particle size for NMC cathode materials. The cracks formation and electrolyte penetration on the secondary NMC particles[26–28] lead to shorter diffusion lengths, and irregular diffusion geometries. The traditional way to tackle this in FSW model is to fit a lumped parameter τ, where

$$\tau = \frac{L^2}{D} \quad [5]$$

τ is often called the characteristic diffusion time constant. Instead of specifying the diffusion thickness, both L and D are evaluated through fitting. Although the τ parameter can also be introduced in PDW, in this work, we use the fixed diffusion length L because L is well-defined for thin-film LNMO electrodes. For the consistency, we also use a fixed L for the analysis of NCA electrodes. However, due to the ambiguity of L for the NCA electrodes, the diffusion coefficients are derived in a semi-quantitative manner, depending on the chosen value of L.

Symmetric cells with identical NCA electrodes at various SOCs were prepared and characterized by ORP-EIS.[8,39] Notably, ORP-EIS can simultaneously evaluate the non-stationarity and non-linearity during EIS measurements, thereby assessing the validity of the EIS spectra. Therefore, the Kramers-Kronig test is no longer necessary. The same set of data has been discussed in our previous work,[8] in which EECM with GFW was applied for the analysis. However, the discussion of the parameters derived from the GFW was preliminary, owing to the limited physical insights given by the model. In this study, we employ a similar EECM approach but use PDW instead of GFW for the analysis. The EECM is shown in Fig. 8a. A constant phase element (CPE) is used to model the dispersive double-layer capacitance due to the porous structure. The impedance of a CPE is given by:

$$Z_{CPE} = \frac{1}{Q(j\omega)^{\alpha}} \quad [6]$$

EIS data at 50% SOC (3.82 V vs Li/Li$^+$) and its fitted data are shown in Figs. 8b and 8c. The major time constant is attributed to the charge transfer resistance coupled with the double-layer capacitance. The low frequency impedance exhibits anomalous diffusion behavior, which can be accurately fitted by the PDW model. The fitting residual is approximately two orders of magnitude lower than the EIS modulus, indicating a generally good fit. The similar fitting quality has been achieved for the entire dataset. The fitted parameters and their relative errors are listed in Table III. Here, all the fittings were performed with a fixed diffusion length L of 300 nm, approximately 1 to 2 times the size of primary particles. This choice was made primarily because the obtained diffusion coefficients are close in magnitude to those from LNMO electrodes. Additionally, different L values were also tested. The fitting results from different L values are shown in the Supplementary Materials (Table S2). When L increases from 150 nm to 750 nm, D_1 and D_2 increase by a factor of 2.5. Other parameters stays the same except Λ, which shows changes with different L values. It might be due to the fitting process.

The plot of R_{ct} as a function of SOC is shown in Fig. 9a. Initially, R_{ct} decreases and then remains at a low level in the middle SOC region. At the high SOC region, R_{ct} increases again. This parabolic-like behavior and the fitting values closely resemble those found in our previous work,[8] where GFW was used for EECM analysis on the same EIS dataset. Similarly, the plots of the fitted CPE parameters, as shown in Supplementary Materials (Fig. S6), closely resemble those from our previous work. For the same dataset, using PDW can yield kinetic parameters that closely match those obtained through the conventional use of GFW. An in-depth discussion of the fitted R_{ct} and CPE values is beyond the scope of this work, however, this information has already been published in our previous work.[8]

Figure 9b presents the plot of the fitted PDW parameters, D_1, D_2, θ, and $1-\theta$, as functions of SOC. Similar to the thin-film LNMO system, the faster diffusion coefficient D_1 is associated with grain boundary diffusion, while D_2 is associated with the slower lattice diffusion. The two diffusion coefficients vary similarly across different SOCs, and the difference is maintained at approximately one order of magnitude. The variation of diffusion coefficients can be attributed to the phase changes of materials at different SOCs. However, further discussion requires a systematic experimental examination, which is planned for future work. Moreover, it is important to note that the diffusion coefficients here are evaluated

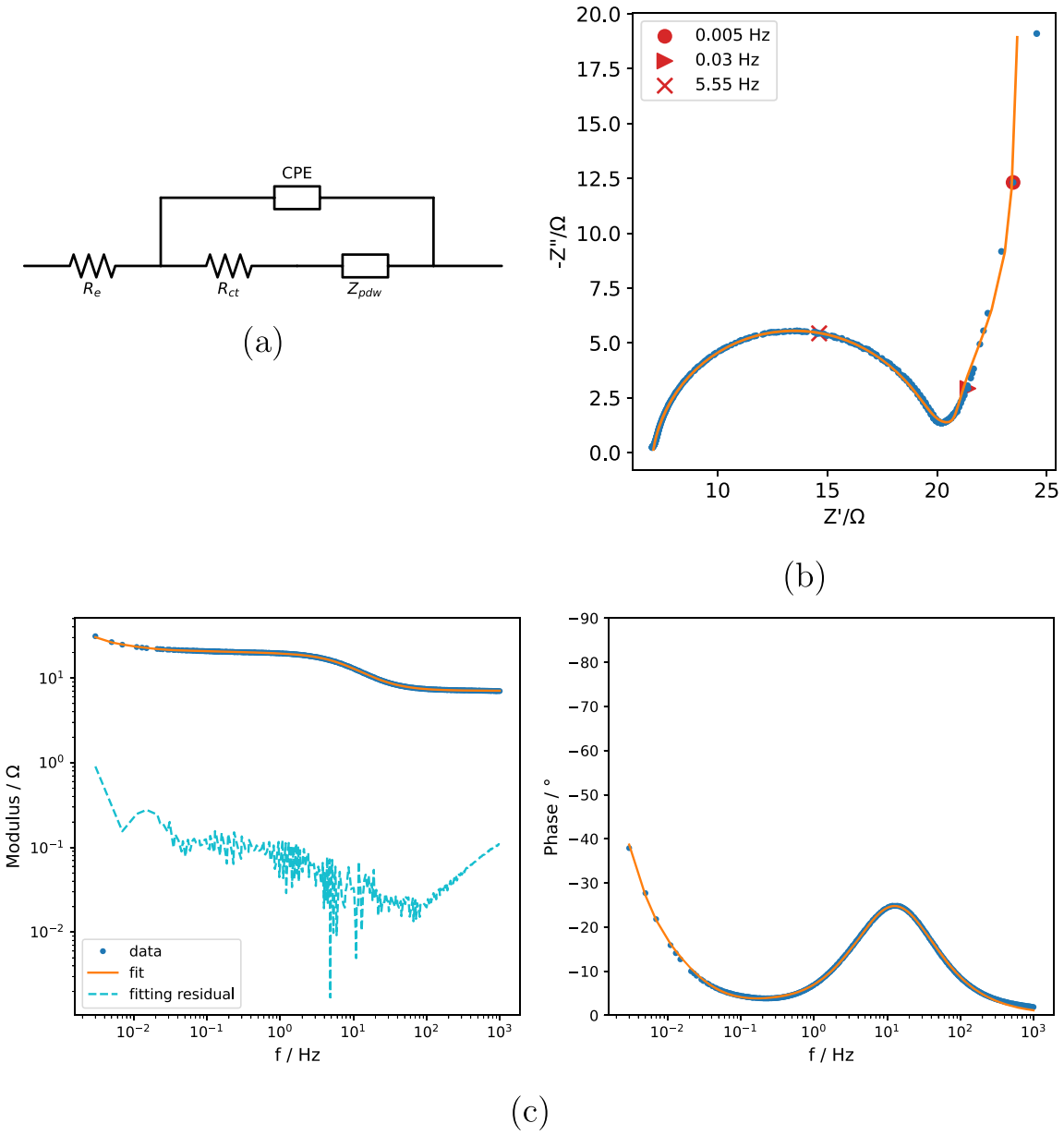

Figure 8. (a) the Randles equivalent circuit model with CPE and PDW integrated; (b) Nyquist plot of EIS data at 50% SOC (3.82 V vs Li/Li$^+$), and its fitted data; (b) Bode plot of the EIS data, the fitted data and the fitting residual. The EIS data is fitted with the EECM of (a); input parameters: $L = 300$ nm; $T = 298.15$ K. Experimental conditions: RMS amplitude of EIS signal is 5 mV; frequency range is 3 mHz–1 kHz.

semi-quantitatively due to the ambiguity of the effective diffusion length for the porous electrodes. Here, we define that L=300 nm for the fitting purpose. However, if L increases (or decreases), the derived diffusion coefficients will increase (or decrease) accordingly. The coverage θ and $1-\theta$ plots are also shown in Fig. 9b. Notably, $1-\theta$, associated with D_2, plays a more dominating role than θ, associated with D_1. This implies that the bulk lattice diffusion plays a major role in the Li$^+$ diffusion of the NCA electrode, which is opposite to the observation in the thin-film LNMO electrode (Fig. 6). We attributed this observation to the presence of moderate density of GBs in the commercial NCA electrodes, as shown in the SEM image Fig. 8a, compared to the thin-film LNMO electrode, which exhibits excessive density of GBs, as shown in Fig. 1a. Figure 9c shows the plot of the lumped parameter Λ versus SOC, where Λ decreases with increasing SOC. This behavior can be directly associated with changes in C_{eq} in different SOCs. Additionally, changes in the active surface area A and the Thermodynamic Factor Γ might also play a role, but it is difficult to assess based on current results. Furthermore, Λ of the NCA electrode is more than one order of magnitude higher than that of the thin-film LNMO electrode. This observation can be attributed to a significant larger active surface area in porous NCA electrodes compared to thin-film LNMO electrodes.

In summary, we have demonstrated that PDW is applicable not only to the analysis of thin-film electrodes but also to conventional porous electrodes. Using the same dataset, PDW can yield fitted kinetic parameters that closely match those obtained through GFW. On top, PDW allows to semi-quantitatively evaluate solid-state diffusion coefficients. Additionally, the surface coverage θ and the parameter Λ (associated with C_{eq}, A, and Γ) could potentially provide extra insights into the solid-state diffusion process, insights that are not available elsewhere. PDW has proven to be an effective alternative to GFW for EECM analysis; however, being aware of PDW's limitations and assumptions is essential for robust analysis.

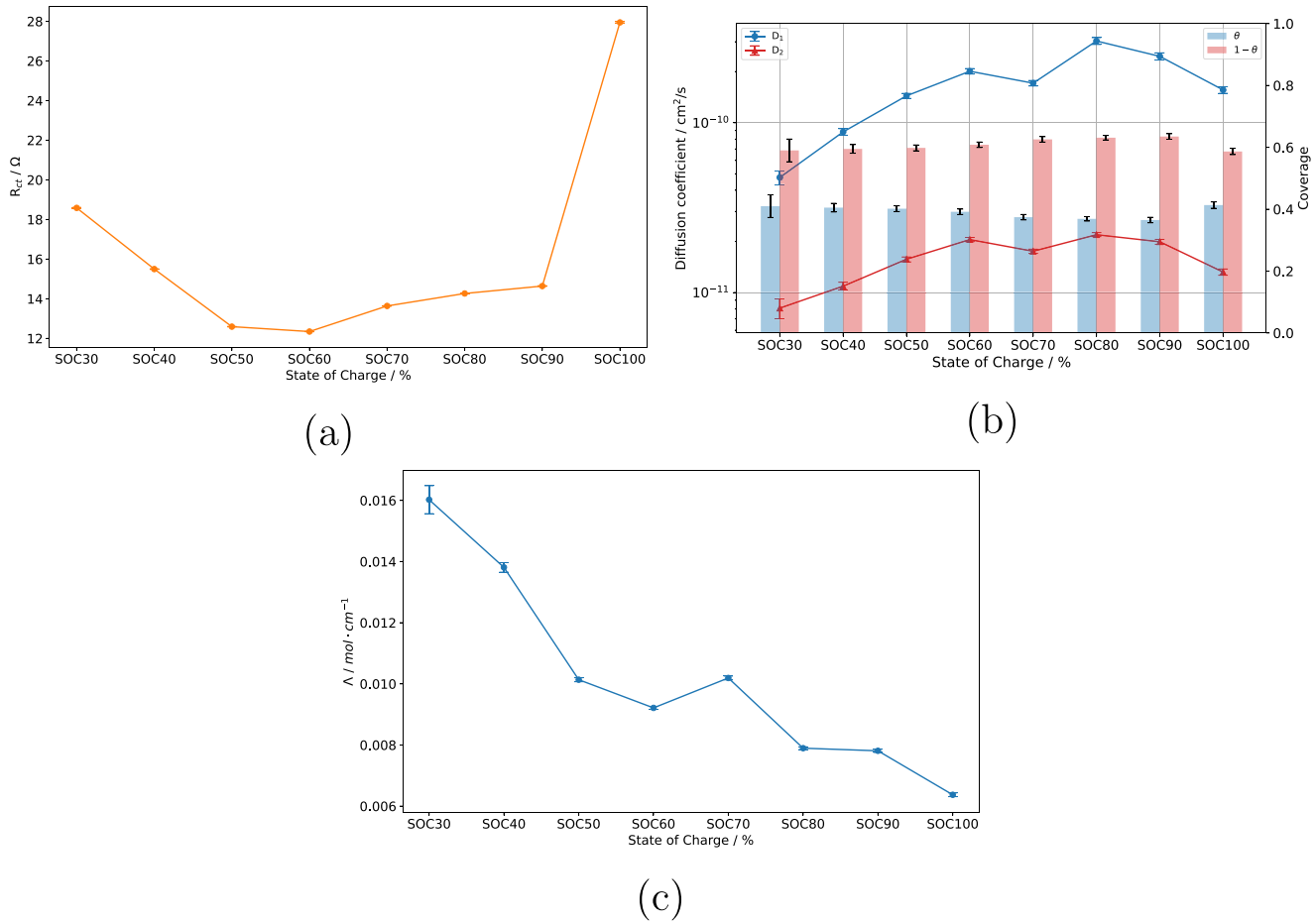

Figure 9. Plots of the fitted parameters and their standard deviation (Table III) as function of electrode potentials. (a) R_{ct}; (b) D_1, D_2 and θ; (c) the lumped parameter Λ.

Table III. Fitted parameter values and their relative errors (in brackets) at various SOCs.

Parameter	SOC30	SOC40	SOC50	SOC60
R_e (Ω)	6.49 (0.1%)	6.24 (0.1%)	7.05 (0.1%)	6.63 (0.1%)
Q ($Fs^{\alpha-1}$)	2.74×10^{-3} (0.5%)	2.83×10^{-3} (0.3%)	2.42×10^{-3} (0.4%)	2.55×10^{-3} (0.4%)
α (-)	0.87 (0.1%)	0.88 (0.1%)	0.91 (0.1%)	0.92 (0.1%)
R_{ct} (Ω)	18.58 (0.2%)	15.50 (0.1%)	12.59 (0.1%)	12.35 (0.1%)
D_1 (cm^2/s)	4.76×10^{-11} (9.2%)	8.83×10^{-11} (4.4%)	1.44×10^{-10} (3.4%)	2.01×10^{-10} (3.7%)
D_2 (cm^2/s)	8.09×10^{-12} (13.6%)	1.09×10^{-11} (5.3%)	1.57×10^{-11} (3.3%)	2.05×10^{-11} (3.0%)
θ (-)	0.41 (8.9%)	0.41 (3.4%)	0.40 (2.3%)	0.39 (2.2%)
Λ (mol/cm)	0.016 (2.8%)	0.014 (1.1%)	0.010 (0.7%)	0.009 (0.6%)
Parameter	SOC70	SOC80	SOC90	SOC100
R_e (Ω)	6.47 (0.1%)	6.28 (0.1%)	6.70 (0.1%)	6.32 (0.1%)
Q ($Fs^{\alpha-1}$)	2.71×10^{-3} (0.3%)	2.67×10^{-3} (0.4%)	2.39×10^{-3} (0.5%)	2.25×10^{-3} (0.3%)
α (-)	0.91 (0.1%)	0.91 (0.1%)	0.94 (0.1%)	0.95 (0.1%)
R_{ct} (Ω)	13.64 (0.1%)	14.27 (0.1%)	14.64 (0.2%)	27.95 (0.1%)
D_1 (cm^2/s)	1.71×10^{-10} (3.7%)	3.03×10^{-10} (4.6%)	2.46×10^{-10} (4.9%)	1.56×10^{-10} (4.5%)
D_2 (cm^2/s)	1.75×10^{-11} (3.0%)	2.19×10^{-11} (2.7%)	1.99×10^{-11} (3.3%)	1.32×10^{-10}(4.4%)
θ (-)	0.37 (2.3%)	0.37 (1.9%)	0.37 (2.4%)	0.41 (2.5%)
Λ (mol/cm)	0.010 (0.6%)	0.008 (0.6%)	0.008 (0.7%)	0.006 (1.0%)

Conclusion

In this study, we first provided a brief overview of the existing approaches to deal with the anomalous solid-state diffusion impedance in LIBs, but there is still a lack of both an easily accessible and physically interpretable analysis method. We then introduced a novel analytical PDW model and coupled it with EECM analysis to tackle the troublesome anomalous solid-state diffusion impedance in LIBs. This novel approach has been successfully demonstrated to analyze both the thin-film LNMO electrodes and porous NCA electrodes. The analytical expression of PDW is derived from the

classical Fickian diffusion framework, introducing non-unified diffusion coefficients originating from the diverse crystalline conditions of Li^+ diffusion paths, as demonstrated in the atomistic modeling results. In practice, PDW with two diffusion coefficients--grain boundary diffusion (fast) and bulk lattice diffusion (slow) - is sufficient for EECM analysis on LIBs. A good understanding of the theoretical assumptions and limitations of PDW model is essential for robust analysis. In future studies, a probability density function of the diffusion coefficient could be introduced to PDW to achieve a more accurate description of the parallel diffusion impedance. Determining the PDF of the diffusion coefficient will be challenging, but could be achieved through more extensive atomistic simulations. This topic will be explored in our future work.

Acknowledgments

This research work is financially supported by SIM (Strategic Initiative Materials)-Flanders through LIFESBAT project and the Research Foundation Flanders(FWO) (Grant No. 1SB6619N). M.H. M acknowledge funding from the Research Foundation–Flanders (FWO, Project 1264221N) and the Flanders Innovation and Entrepreneurship (VLAIO, Project number: HBC.2021.0017). The computational resources and services used in this work were provided by the VSC (Flemish Supercomputer Center), under grant number gpr-compute-2024-016, funded by the Research Foundation Flanders (FWO) and the Flemish Government. The authors acknowledge Jun Huang and Noël Hallemans for the fruitful discussions. ChatGPT 4.0 has been used solely for proofreading purposes in this manuscript.

Appendix A. Theory of Parallel-diffusion Warburg Model

When small potential perturbation ΔE is applied in EIS measurements, the concentration changes accordingly $C(x, t) = C_{eq} + \Delta c(x, t)$. At the electrode/electrolyte interface ($x = 0$), the change of activity $a(t)$ can be described by Nernst euqation Eq. A·1, which can be simplified to a linear form for a small perturbation.[50] R is the gas constant, T is the temperature in Kelvin, z is the number of electrons transferred, F is the Faraday constant, and a_{eq} is the activity at the equilibrium state.

$$\Delta E(t) = \frac{RT}{zF}\ln\frac{a_{eq} + \Delta a(t)}{a_{eq}} \approx \frac{RT}{zFa_{eq}}\Delta a(t) \qquad [A\cdot1]$$

The relation between activity and concentration is given through Eq. A·2,[60] where the Thermodynamic Factor (or Darken factor).[50,54] $\Gamma = d\ln a/d\ln C$.

$$\frac{\Delta a}{\Delta c} \approx \frac{da}{dC} = \frac{a}{C}\cdot\frac{d\ln a}{d\ln C} = \frac{a}{C}\Gamma \qquad [A\cdot2]$$

Accordingly, Eq. A·3 is derived.

$$\Delta E(t) = \frac{RT\Gamma}{zFC_{eq}}\Delta c(x, t)\Big|_{x=0} \qquad [A\cdot3]$$

For the simplicity, the Laplace transform of Eq. A·3 is Eq. A·4, with s as Laplace variable.

$$\Delta E(s) = \frac{RT\Gamma}{zFC_{eq}}\Delta c(x, s)\Big|_{x=0} \qquad [A\cdot4]$$

The impedance in Laplace space can be simply defined as Eq. A·5.

$$Z(s) = \Delta E(s)/I(s) \qquad [A\cdot5]$$

The current response $I(s)$ is associated with chemical diffusion process through Eq. A·6, where A is the active surface area and $J(s)$ is the flux of diffusion species.

$$I(s) = zFAJ(s)|_{x=0} \qquad [A\cdot6]$$

At the electrode/electrolyte interface ($x = 0$), the flux can be described by Fick's first law as shown in Eq. A·7, with $\tilde{D}$ as the chemical diffusion coefficient.

$$J(s) = -\tilde{D}\frac{d\Delta c(x, s)}{dx}\Big|_{x=0} \qquad [A\cdot7]$$

The Fick's second law is given in Eq. A·8 with the boundary condition of Eq. A·9, which manifests finite-length diffusion with an impermeable boundary ($x = L$). It is important to mention that Eqs. A·7–A·9 are in the Laplace space.[10,61]

$$s\cdot\Delta c(x, s) = \tilde{D}\frac{\partial^2\Delta c(x, s)}{\partial x^2} \qquad [A\cdot8]$$

$$\frac{\partial\Delta c(x, s)}{\partial x}\Big|_{x=L} = 0 \qquad [A\cdot9]$$

The general solution of Eq. A·8 is given by Eq. A·10.[10,57,60]

$$\Delta c(x, s) = \xi\sinh\left(x\sqrt{\frac{s}{\tilde{D}}}\right) + \zeta\cosh\left(x\sqrt{\frac{s}{\tilde{D}}}\right) \qquad [A\cdot10]$$

This leads to a new expression for the Fick's first law given in Eq. A·11.

$$J(s) = -\tilde{D}\left[\xi\sqrt{\frac{s}{\tilde{D}}}\cosh\left(x\sqrt{\frac{s}{\tilde{D}}}\right) + \zeta\sqrt{\frac{s}{\tilde{D}}}\sinh\left(x\sqrt{\frac{s}{\tilde{D}}}\right)\right]\Big|_{x=0} = -\tilde{D}\xi\sqrt{\frac{s}{\tilde{D}}} \qquad [A\cdot11]$$

From the boundary condition Eq. A·9 at $x = L$, we can derive Eq. A·12.

$$\zeta = -\xi\cdot\coth(L\sqrt{\frac{s}{\tilde{D}}}) \qquad [A\cdot12]$$

Based on Eq. A·10 - A·12 and Eq. A·6, we can derive Eq. A·13, which manifests a correlation between $\Delta c(x, s)$ and $J(s)$ at the electrode/electrolyte interface ($x = 0$).

$$\Delta c(x, s) = \frac{J(s)}{\sqrt{s\tilde{D}}}\cdot\coth\left(L\sqrt{\frac{s}{\tilde{D}}}\right)\Big|_{x=0} \qquad [A\cdot13]$$

Now the impedance $Z(s)$ can be written in the form of Eq. A·14.

$$Z(s) = \frac{\Delta E(s)}{I(s)} = \frac{\Delta E(s)}{zFAJ(s)} = \frac{RT\Gamma}{z^2F^2C_{eq}}\cdot\frac{\Delta c(x, s)}{AJ(s)}\Big|_{x=0} \qquad [A\cdot14]$$

Here, we can introduce two parallel chemical diffusion process with two diffusion coefficient$\tilde{D}_1$ and $\tilde{D}_2$, then two flux $J_1(s)$ and $J_2(s)$ are presence in the diffusion process as well. Accordingly, the impedance $Z(s)$ can be expressed in the form of Eq. A·15, where the θ ($0 \leqslant \theta \leqslant 1$) and $1 - \theta$ are the surface coverage of the two parallel diffusion process, respectively.

$$Z(s) = \frac{RT\Gamma}{z^2F^2C_{eq}}\cdot\frac{\Delta c(x, s)}{\theta AJ_1(s) + (1-\theta)AJ_2(s)}\Big|_{x=0} \qquad [A\cdot15]$$

Insert Eq. A·13 and replace s with $j\omega$ (under a steady state), we can derive the final expression of the parallel-diffusion Warburg impedance $Z_{pdw}(\omega)$ in Eq. A·16.

$$Z_{pdw}(\omega) = \frac{RT\Gamma}{z^2F^2C_{eq}A} \cdot \frac{1}{\theta\sqrt{j\omega\tilde{D}_1}\tanh\left(L\sqrt{\frac{j\omega}{\tilde{D}_1}}\right) + (1-\theta)\sqrt{j\omega\tilde{D}_2}\tanh\left(L\sqrt{\frac{j\omega}{\tilde{D}_2}}\right)} \quad [A\cdot16]$$

ORCID

Xinhua Zhu https://orcid.org/0000-0002-8919-1557
Marta Cazorla Soult https://orcid.org/0000-0001-7350-0127

References

1. E. Barsoukov and J. R. Macdonald, *Impedance Spectroscopy: Theory, Experiment, and Applications* (Wiley) (2018).
2. M. Kuipers, P. Schröer, T. Nemeth, H. Zappen, A. Blömeke, and D. U. Sauer, "An algorithm for an online electrochemical impedance spectroscopy and battery parameter estimation: development, verification and validation." *Journal of Energy Storage*, **30**, 101517 (2020).
3. S. M. Islam and S. Y. Park, "Precise online electrochemical impedance spectroscopy strategies for li-ion batteries." *IEEE Transactions on Industry Applications*, **56**, 1661 (2020).
4. M. Crescentini, A. De Angelis, R. Ramilli, G. De Angelis, M. Tartagni, A. Moschitta, P. A. Traverso, and P. Carbone, "Online EIS and diagnostics on lithium-ion batteries by means of low-power integrated sensing and parametric modeling." *IEEE Trans. Instrum. Meas.*, **70**, 1 (2021).
5. X. Zhu, N. Hallemans, B. Wouters, R. Claessens, J. Lataire, and A. Hubin, "Operando odd random phase electrochemical impedance spectroscopy as a promising tool for monitoring lithium-ion batteries during fast charging." *Journal of Power Sources*, **544**, 231852 (2022).
6. M. Gaberšček, "Impedance spectroscopy of battery cells: Theory versus experiment." *Current Opinion in Electrochemistry*, **32**, 100917 (2022).
7. J. P. Schmidt, T. Chrobak, M. Ender, J. Illig, D. Klotz, and E. Ivers-Tiffée, "Studies on lifepo4 as cathode material using impedance spectroscopy." *Journal of Power Sources*, **196**, 5342 (2011).
8. X. Zhu, L. F. Macía, J. Jaguemont, J. de Hoog, A. Nikolian, N. Omar, and A. Hubin, "Electrochemical impedance study of commercial lini0.80-co0.15al0.05o2 electrodes as a function of state of charge and aging." *Electrochimica Acta*, **287**, 10 (2018).
9. C. Ho, I. D. Raistrick, and R. A. Huggins, "Application of a-c techniques to the study of lithium diffusion in tungsten trioxide thin films." *J. Electrochem. Soc.*, **127**, 343 (1980).
10. I. RAISTRICK and R. HUGGINS, "The transient electrical response of electrochemical systems containing insertion reaction electrodes." *Solid State Ionics*, **7**, 213 (1982).
11. B. Boukamp and G. Wiegers, "Ionic and electronic processes in agcrse2." *Solid State Ionics*, **9-10**, 1193 (1983).
12. C. Gabrielli, P. P. Grand, A. Lasia, and H. Perrot, "Investigation of hydrogen adsorption and absorption in palladium thin films." *J. Electrochem. Soc.*, **151**, A1943 (2004).
13. S. Erol and M. E. Orazem, "The influence of anomalous diffusion on the impedance response of licoo2|c batteries." *Journal of Power Sources*, **293**, 57 (2015).
14. V. Charbonneau, A. Lasia, and G. Brisard, "Impedance studies of li+ diffusion in nickel manganese cobalt oxide (nmc) during charge/discharge cycles." *Journal of Electroanalytical Chemistry*, **875**, 113944 (2020).
15. J. R. Macdonald, "Frequency response of unified dielectric and conductive systems involving an exponential distribution of activation energies." *J. Appl. Phys.*, **58**, 1955 (1985).
16. J. Huang, "Diffusion impedance of electroactive materials, electrolytic solutions and porous electrodes: warburg impedance and beyond." *Electrochimica Acta*, **281**, 170 (2018).
17. J. Bisquert and A. Compte, "Theory of the electrochemical impedance of anomalous diffusion." *Journal of Electroanalytical Chemistry*, **499**, 112 (2001).
18. J. Bisquert, "Interpretation of a fractional diffusion equation with nonconserved probability density in terms of experimental systems with trapping or recombination." *Physical Review E–Statistical, Nonlinear, and Soft Matter Physics*, **72**, 011109 (2005).
19. J. R. Macdonald, "Utility of continuum diffusion models for analyzing mobile-ion immittance data: electrode polarization, bulk, and generation-recombination effects." *Journal of Physics Condensed Matter*, **22**, 495101 (2010).
20. J. R. MacDonald, L. R. Evangelista, E. K. Lenzi, and G. Barbero, "Comparison of impedance spectroscopy expressions and responses of alternate anomalous poisson-nernst-planck diffusion equations for finite-length situations." *J. Phys. Chem. C*, **115**, 7648 (2011).
21. M. D. Levi, C. Wang, and D. Aurbach, "Two parallel diffusion paths model for interpretation of pitt and eis responses from non-uniform intercalation electrodes." *Journal of Electroanalytical Chemistry*, **561**, 1 (2004).
22. T. Osaka, T. Momma, D. Mukoyama, and H. Nara, "Proposal of novel equivalent circuit for electrochemical impedance analysis of commercially available lithium ion battery." *Journal of Power Sources*, **205**, 483 (2012).
23. J.-P. Diard, B. L. Gorrec, and C. Montella, "Influence of particle size distribution on insertion processes in composite electrodes. potential step and eis theory." *Journal of Electroanalytical Chemistry*, **499**, 67 (2001).
24. J. Song and M. Z. Bazant, "Effects of nanoparticle geometry and size distribution on diffusion impedance of battery electrodes." *J. Electrochem. Soc.*, **160**, A15 (2013).
25. J. Min, L. M. Gubow, R. J. Hargrave, J. B. Siegel, and Y. Li, "Direct measurements of size-independent lithium diffusion and reaction times in individual polycrystalline battery particles." *Energy Environmental Science*, **16**, 3847 (2023).
26. E. Trevisanello, R. Ruess, G. Conforto, F. H. Richter, and J. Janek, "Polycrystalline and single crystalline ncm cathode materialsquantifying particle cracking, active surface area, and lithium diffusion." *Adv. Energy Mater.*, **11**, 2003400 (2021).
27. X. Zhu, R. I. Revilla, J. Jaguemont, J. V. Mierlo, and A. Hubin, "Insights into cycling aging of lini 0.80 co 0.15 al 0.05 o 2 cathode induced by surface inhomogeneity: a post-mortem analysis." *The Journal of Physical Chemistry C*, **123**, 30046 (2019).
28. R. Ruess, S. Schweidler, H. Hemmelmann, G. Conforto, A. Bielefeld, D. A. Weber, J. Sann, M. T. Elm, and J. Janek, "Influence of ncm particle cracking on kinetics of lithium-ion batteries with liquid or solid electrolyte." *J. Electrochem. Soc.*, **167**, 100532 (2020).
29. G. Sikha and R. E. White, "Analytical expression for the impedance response of an insertion electrode cell." *J. Electrochem. Soc.*, **154**, A43 (2007).
30. G. Sikha and R. E. White, "Analytical expression for the impedance response for a lithium-ion cell." *J. Electrochem. Soc.*, **155**, A893 (2008).
31. J. Huang, Z. Li, J. Zhang, S. Song, Z. Lou, and N. Wu, "An analytical three-scale impedance model for porous electrode with agglomerates in lithium-ion batteries." *J. Electrochem. Soc.*, **162**, A585 (2015).
32. J. Huang and J. Zhang, "Theory of impedance response of porous electrodes: Simplifications, inhomogeneities, non-stationarities and applications." *J. Electrochem. Soc.*, **163**, A1983 (2016).
33. J. Huang, Y. Gao, J. Luo, S. Wang, C. Li, S. Chen, and J. Zhang, "Editors' choicereviewimpedance response of porous electrodes: Theoretical framework, physical models and applications." *J. Electrochem. Soc.*, **167**, 166503 (2020).
34. E. Woillez and M. Chandesris, "Insight into lib diffusion phenomena using analytical impedance models." *J. Electrochem. Soc.*, **170**, 070527 (2023).
35. J. Huang, "Generalization of porous electrode theory for noninteger dimensional space." *The Journal of Physical Chemistry C*, **122**, 557 (2018).
36. M. C. Soult, V. Siller, X. Zhu, R. Gehlhaar, P. J. Wojcik, A. Morata, A. Tarancón, P. M. Vereecken, and A. Hubin, "Spectroscopic ellipsometry for operando monitoring of (de)lithiation-induced phenomena on $LiMn_2O_4$ and $LiNi_{0.5}Mn_{1.5}O_4$ electrodes." *J. Electrochem. Soc.*, **169**, 040501 (2022).
37. M. C. Soult, A. I. P. Martinez, K. Marcoen, X. Zhu, A. Hubin, and P. M. Vereecken, "Revealing the role of electrolyte salt decomposition in the structural breakdown of $LiNi_{0.5}Mn_{1.5}O_4$." *The Journal of Physical Chemistry C*, **127**, 17637 (2023).
38. N. Hallemans, W. D. Widanage, X. Zhu, S. Moharana, M. Rashid, A. Hubin, and J. Lataire, "Operando electrochemical impedance spectroscopy and its application to commercial li-ion batteries." *Journal of Power Sources*, **547**, 232005 (2022).
39. N. Hallemans, D. Howey, A. Battistel, N. F. Saniee, F. Scarpioni, B. Wouters, F. L. Mantia, A. Hubin, W. D. Widanage, and J. Lataire, "Electrochemical impedance spectroscopy beyond linearity and stationarity–a critical review." *Electrochimica Acta*, **466**, 142939 (2023).
40. M. Schönleber, D. Klotz, and E. Ivers-Tiffée, "A method for improving the robustness of linear kramers-kronig validity tests." *Electrochimica Acta*, **131**, 20 (2014).
41. M. Murbach, B. Gerwe, and N. Dawson-Elli, "L. kun Tsui, impedance.py: a python package for electrochemical impedance analysis." *Journal of Open Source Software*, **5**, 2349 (2020).
42. M. Newville et al., (2024) lmfit/lmfit–py: 1.3.110.5281/zenodo.10998841.
43. C. Chen and S. P. Ong, "A universal graph deep learning interatomic potential for the periodic table." *Nature Computational Science*, **2**, 718 (2022).
44. R. Rüger, M. Franchini, T. Trnka, A. Yakovlev, E. van Lenthe, P. Philipsen, T. van Vuren, B. Klumpers, and T. Soini, *Ams 2023.1, Scm, Theoretical Chemistry* (Vrije Universiteit, Amsterdam, The Netherlands) (2021).
45. S. Takamoto et al., "Towards universal neural network potential for material discovery applicable to arbitrary combination of 45 elements." *Nat. Commun.*, **13**, 2991 (2022).
46. X. He, H. Sun, X. Ding, and K. Zhao, "Grain boundaries and their impact on li kinetics in layered-oxide cathodes for li-ion batteries." *Journal of Physical Chemistry C*, **125**, 10284 (2021).
47. S. Smidstrup, T. Markussen, P. Vancraeyveld, J. Wellendorff, J. Schneider, T. Gunst, B. Verstichel, D. Stradi, P. Khomyakov, and U. Vej-Hansen, "Quantumatk: an integrated platform of electronic and atomic-scale modelling tools." *J. Phys.: Condens. Matter*, **32**, 015901 (2019).
48. F. Fiesinger, D. Gaissmaier, M. van den Borg, J. Beßner, A. C. T. van Duin, and T. Jacob, "Development of a Mg/O reaxff potential to describe the passivation processes in magnesium-ion batteries." *ChemSusChem*, **16**, e202201821 (2023).
49. G. Henkelman, B. P. Uberuaga, and H. Jónsson, "A climbing image nudged elastic band method for finding saddle points and minimum energy paths." *The Journal of Chemical Physics*, **113**, 9901 (2000).
50. W. Weppner and R. A. Huggins, "Determination of the kinetic parameters of mixed-conducting electrodes and application to the system Li_3Sb." *J. Electrochem. Soc.*, **124**, 1569 (1977).
51. T. Mütschele and R. Kirchheim, "Segregation and diffusion of hydrogen in grain boundaries of palladium." *Scripta Metallurgica*, **21**, 135 (1987).

52. J. Horváth, R. Birringer, and H. Gleiter, "Diffusion in nanocrystalline material." *Solid State Commun.*, **62**, 319 (1987).
53. S. Han, J. Park, W. Lu, and A. M. Sastry, "Numerical study of grain boundary effect on li+ effective diffusivity and intercalation-induced stresses in li-ion battery active materials." *Journal of Power Sources*, **240**, 155 (2013).
54. L. S. Darken, "Diffusion, mobility and their interrelation through free energy in binary metallic systems." *Trans. Aime*, **175**, 184 (1948).
55. J. E. B. Randles, "Kinetics of rapid electrode reactions." *Discuss. Faraday Soc.*, **1**, 11 (1947).
56. M. Ingdal, R. Johnsen, and D. A. Harrington, "The akaike information criterion in weighted regression of immittance data." *Electrochimica Acta*, **317**, 648 (2019).
57. A. Lasia, *Electrochemical Impedance Spectroscopy and its Applications* (Springer, New York) (2014).
58. A. J. Bard, L. R. Faulkner, and H. S. White, *Electrochemical Methods: Fundamentals and Applications* (Wiley, New York) (2022).
59. N. Ogihara, Y. Itou, T. Sasaki, and Y. Takeuchi, "Impedance spectroscopy characterization of porous electrodes under different electrode thickness using a symmetric cell for high-performance lithium-ion batteries–supporting information." *Journal of Physical Chemistry C*, **119**, 4612 (2015).
60. B. A. Boukamp, "Derivation of a distribution function of relaxation times for the (fractal) finite length warburg." *Electrochimica Acta*, **252**, 154 (2017).
61. J. Crank, *The Mathematics of Diffusion* (Oxford University Press, Oxford) (1979).